



# Thermochemistry of Calcium-Magnesium-Aluminum-Silicate (CMAS) and Components of Advanced Thermal and Environmental Barrier Coating Systems

*Gustavo C. C. Costa*

*Vantage Partners, LLC, Brook Park, Ohio*

*Waldo A. Acosta*

*U.S. Army Research Laboratory, Glenn Research Center, Cleveland, Ohio*

*Dongming Zhu*

*Glenn Research Center, Cleveland, Ohio*

*Anindya Ghoshal*

*U.S. Army Research Laboratory, Adelphi, Maryland*

## NASA STI Program . . . in Profile

Since its founding, NASA has been dedicated to the advancement of aeronautics and space science. The NASA Scientific and Technical Information (STI) Program plays a key part in helping NASA maintain this important role.

The NASA STI Program operates under the auspices of the Agency Chief Information Officer. It collects, organizes, provides for archiving, and disseminates NASA's STI. The NASA STI Program provides access to the NASA Technical Report Server—Registered (NTRS Reg) and NASA Technical Report Server—Public (NTRS) thus providing one of the largest collections of aeronautical and space science STI in the world. Results are published in both non-NASA channels and by NASA in the NASA STI Report Series, which includes the following report types:

- **TECHNICAL PUBLICATION.** Reports of completed research or a major significant phase of research that present the results of NASA programs and include extensive data or theoretical analysis. Includes compilations of significant scientific and technical data and information deemed to be of continuing reference value. NASA counter-part of peer-reviewed formal professional papers, but has less stringent limitations on manuscript length and extent of graphic presentations.
- **TECHNICAL MEMORANDUM.** Scientific and technical findings that are preliminary or of specialized interest, e.g., “quick-release” reports, working papers, and bibliographies that contain minimal annotation. Does not contain extensive analysis.
- **CONTRACTOR REPORT.** Scientific and technical findings by NASA-sponsored contractors and grantees.
- **CONFERENCE PUBLICATION.** Collected papers from scientific and technical conferences, symposia, seminars, or other meetings sponsored or co-sponsored by NASA.
- **SPECIAL PUBLICATION.** Scientific, technical, or historical information from NASA programs, projects, and missions, often concerned with subjects having substantial public interest.
- **TECHNICAL TRANSLATION.** English-language translations of foreign scientific and technical material pertinent to NASA's mission.

For more information about the NASA STI program, see the following:

- Access the NASA STI program home page at <http://www.sti.nasa.gov>
- E-mail your question to [help@sti.nasa.gov](mailto:help@sti.nasa.gov)
- Fax your question to the NASA STI Information Desk at 757-864-6500
- Telephone the NASA STI Information Desk at 757-864-9658
- Write to:  
NASA STI Program  
Mail Stop 148  
NASA Langley Research Center  
Hampton, VA 23681-2199



# Thermochemistry of Calcium-Magnesium-Aluminum-Silicate (CMAS) and Components of Advanced Thermal and Environmental Barrier Coating Systems

*Gustavo C. C. Costa*

*Vantage Partners, LLC, Brook Park, Ohio*

*Waldo A. Acosta*

*U.S. Army Research Laboratory, Glenn Research Center, Cleveland, Ohio*

*Dongming Zhu*

*Glenn Research Center, Cleveland, Ohio*

*Anindya Ghoshal*

*U.S. Army Research Laboratory, Adelphi, Maryland*

National Aeronautics and  
Space Administration

Glenn Research Center  
Cleveland, Ohio 44135

## Acknowledgments

We are grateful to R. Rogers (NASA Glenn) for assistance with X-ray diffraction.

This report contains preliminary findings,  
subject to revision as analysis proceeds.

Trade names and trademarks are used in this report for identification  
only. Their usage does not constitute an official endorsement,  
either expressed or implied, by the National Aeronautics and  
Space Administration.

This work was sponsored by the  
Transformative Aeronautics Concepts Program.

*Level of Review:* This material has been technically reviewed by technical management.

Available from

NASA STI Program  
Mail Stop 148  
NASA Langley Research Center  
Hampton, VA 23681-2199

National Technical Information Service  
5285 Port Royal Road  
Springfield, VA 22161  
703-605-6000

This report is available in electronic form at <http://www.sti.nasa.gov/> and <http://ntrs.nasa.gov/>

# **Thermochemistry of Calcium-Magnesium-Aluminum-Silicate (CMAS) and Components of Advanced Thermal and Environmental Barrier Coating Systems**

Gustavo C. C. Costa  
Vantage Partners, LLC  
Brook Park, Ohio 44142

Waldo A. Acosta  
U.S. Army Research Laboratory  
Glenn Research Center  
Cleveland, Ohio 44135

Dongming Zhu  
National Aeronautics and Space Administration  
Glenn Research Center  
Cleveland, Ohio 44135

Anindya Ghoshal  
U.S. Army Research Laboratory  
Adelphi, Maryland 20783

## **Summary**

There is increasing interest in the degradation mechanism studies of thermal and environmental barrier coatings (TEBCs) of gas turbines by molten calcium-magnesium-aluminum-silicate ( $\text{CaO-MgO-Al}_2\text{O}_3\text{-SiO}_2$ , CMAS). CMAS minerals are usually referred to as silicon-containing sand dust and volcano ash materials that are carried by the intake air into gas turbines (e.g., in aircraft engines), and their deposits often react at high temperatures ( $>1200^\circ\text{C}$ ) with the engine turbine coating systems and components. The high-temperature reactions cause degradation and accelerated failure of the static and rotating components of the turbine engines. Some results of the reactions between the CMAS and rare-earth (RE = Y, Yb, Dy, Gd, Nd, and Sm)-oxide-stabilized  $\text{ZrO}_2$  or  $\text{HfO}_2$  systems are discussed as well as the stability of the resulting oxides and silicates. Plasma-sprayed hollow-tube samples (outside diameter  $\varnothing = 4.7$  mm, wall thickness = 0.76 mm, and height = 26 mm) were half filled with CMAS powder, wrapped and sealed with platinum foil, and heat treated at  $1310^\circ\text{C}$  for 5 h. Samples were characterized by differential scanning calorimetry, X-ray diffraction, electron microscopy analysis of cross sections, and energy dispersive X-ray spectroscopy. It was found that CMAS penetrated the samples at the grain boundaries and dissolved the TEBC materials to form silicate phases containing the RE elements. Furthermore, it was found that apatite crystalline phases were formed in the samples with total RE content higher than 12 mol% in the reaction zone for the  $\text{ZrO}_2$  system. In general, samples with the nominal compositions 30% yttria-stabilized zirconia (30YSZ),  $\text{HfO}_2\text{-7Dy}_2\text{O}_3$ , and  $\text{ZrO}_2\text{-9.5Y}_2\text{O}_3\text{-2.25Gd}_2\text{O}_3\text{-2.25Yb}_2\text{O}_3$  exhibited lower reactivity or more resistance to CMAS than the other coating compositions of this work.

## **Introduction**

Thermal and environmental barrier coatings (TEBCs) are critical for next-generation turbine engines because of their ability to allow the implementation of lightweight and high-temperature SiC/SiC engine ceramic matrix composite (CMC) components (Refs. 1 and 2). The incorporation of SiC/SiC CMC hot-section components in high-pressure turbine engine systems will enable engine designs with higher

inlet temperatures, higher thrust-to-weight ratio, and reduced cooling, thus helping to significantly improve engine efficiency and performance. However, a prime-reliant coating system design approach is particularly important to implement the CMC technology in the turbine engine systems to fully protect the ceramic components in combustion and harsh operation environments. In particular, in order to meet the environmental barrier coating (EBC) protection requirements to prevent the SiC/SiC CMC from water vapor attack for in-turbine-engine combustion environments (Refs. 1, 3, and 4), advanced ZrO<sub>2</sub>, HfO<sub>2</sub>, and rare earth (RE) silicate EBC systems have also been proposed as candidate coating materials to improve temperature capability and environmental protection of SiC/SiC CMCs because of their exceptional stabilities in the turbine combustion environments (Refs. 1, 5, and 6).

The significantly higher operating temperatures envisioned for next-generation turbine engine hot-section CMC components impose significant material design challenges and also raise serious component environmental durability issues. During engine operation, entrained road-sand calcium-magnesium-aluminum-silicate (CaO-MgO-Al<sub>2</sub>O<sub>3</sub>-SiO<sub>2</sub>, CMAS) deposits on the turbine TEBCs and components form glassy melts, which can significantly reduce the TEBC and silicon-based ceramic component temperature capability. It is critical to understand the high-temperature interactions between the coating materials and CMAS in order to develop advanced CMAS-resistant coatings. Some more recent work has been done to determine the mechanisms by which CMAS can cause failure and performance degradations in yttria-stabilized zirconia (YSZ) thermal barrier coatings (TBCs) and RE silicate TEBCs (Refs. 7 to 13).

The objective of this report is to investigate the thermochemistry reactions and stability of advanced plasma-spray-processed ZrO<sub>2</sub> and HfO<sub>2</sub> TEBCs in contact with CMAS at high temperature. Although the ZrO<sub>2</sub> and HfO<sub>2</sub> systems have been used and classified as a TBC material, this report explores the possibility of improving these ceramic systems containing RE elements in an EBC system. Thus, these advanced coating systems are named here “thermal and environmental barrier coatings,” or TEBCs. A particular emphasis has been placed on the effect of yttria and RE dopants on the CMAS resistance in the advanced ZrO<sub>2</sub> and HfO<sub>2</sub> systems, and on correlating with the dopant oxides. The information will also help in understanding the reaction mechanisms of ZrO<sub>2</sub> and HfO<sub>2</sub>, which may help in developing a more CMAS-resistant coating system for CMC components in next-generation turbine engines.

## **Experimental Materials and Methods**

### **Materials**

Ceramic powders based on rare-earth- (RE = Y, Yb, Dy, Gd, Nd, and Sm) oxide-stabilized ZrO<sub>2</sub> or HfO<sub>2</sub> systems were air plasma sprayed onto 1/8-in. Ø graphite bar substrates to form 0.030-in.-thick coatings. These materials were selected because they have been developed as low-conductivity TBCs for turbine engine applications (Ref. 14). The air-plasma-sprayed specimens were sintered at 1500 °C for 5 h, resulting in hollow-tube samples (outside diameter Ø = 4.7 mm, wall thickness = 0.76 mm, and height = 26 mm). Following sintering, the samples were half filled with NASA-composition CMAS powder (Ref. 15) synthesized by Washington Mills Ceramics Corporation (Sun Prairie, WI) using NASA specifications, wrapped and sealed with platinum foil, and heat treated at 1310 °C for 5 h. All the samples, including the hollow tubes and NASA CMAS, were characterized before and after reaction by differential scanning calorimetry (DSC), X-ray diffraction (XRD), and electron microscopy analysis of cross sections (details of the characterization techniques are given in the Sample Characterization section).

### **Sample Characterization**

The sintered hollow-tube specimens were analyzed by helium pycnometry and by nitrogen adsorption in a surface characterization analyzer (3Flex, Micrometrics Instrument Corporation, Norcross, GA). The pristine NASA composition CMAS and the reacted hollow-tube samples with CMAS were ground in an agate mortar and analyzed by XRD on a Bruker D8 Discover diffractometer (Bruker-AXS GmbH, Karlsruhe, Germany). The NASA pristine powder was also characterized by nitrogen adsorption;

inductively coupled plasma optical emission spectroscopy (ICP–OES) at NSL Labs, Cleveland, OH; field emission scanning electron microscopy (FE–SEM) Hitachi S–4700–II (Hitachi High Technologies, Gaithersburg, MD) equipped with energy dispersive X-ray spectroscopy (EDS) (EDAX, Mahwah, NJ), secondary electron (SE), and backscatter electron (BSE) detectors; and differential scanning calorimetry (DSC) thermal analysis using a Netzsch Model F1 Pegasus® calorimeter (Netzsch GmbH, Selb, Germany). The evolution of the reaction between NASA composition CMAS and ZrO<sub>2</sub>-30Y<sub>2</sub>O<sub>3</sub> powder samples (1:2 mass ratio) was also characterized by DSC thermal analysis. The lower and upper section of the reacted hollow-tube samples were cut at approximately 3 mm from their end and mounted in a PolyFast® resin (Struers), polished using a nonaqueous solution. The mounted samples were carbon coated and analyzed by FE–SEM coupled with EDS.

## Results

The composition of the sintered hollow-tube samples (Table I) analyzed by EDS are similar to the nominal compositions. The EDS analysis of the samples was performed at 30 kV, and the amount of zirconium and yttrium was obtained from their K $\alpha$  lines since they do not overlap. Instead of coating the samples, a charge compensator probe was used to dissipate charging at their surface.

Table II shows the initial parameters of the hollow-tube samples (Brunauer-Emmet-Teller (BET) specific surface area, density, surface area and total volume of pores, and CMAS surface concentration) measured by N<sub>2</sub> gas adsorption, He picnometry, and geometric and gravimetric methods. The samples are well sintered, and their relative density ( $\rho_{\text{geometric}} \cdot 100 / \rho_{\text{helium}}$ ) ranges from 90 to 100 percent. The specific surface area of the hollow tubes are also very low (<0.01 to 0.3 m<sup>2</sup>/g), indicating that the samples are well sintered. The samples also exhibit very small pore volume ( $3 \times 10^{-5}$  to  $30 \times 10^{-5}$  cm<sup>3</sup>/g) and surface area (0.001 to 0.16 m<sup>2</sup>/g).

Table III shows a comparison of the composition of NASA CMAS measured by EDS and ICP–OES analyses. The NASA CMAS compositions measured by EDS and ICP–OES are the same—within the experimental error—with the exception of Al<sub>2</sub>O<sub>3</sub>, which is slightly different: the Al<sub>2</sub>O<sub>3</sub> content measured by EDS is  $1.9 \pm 0.8$  mol% higher than that measured by ICP–OES.

Figure 1 shows the XRD pattern of the as-received CMAS powder. The as-received CMAS sample analyzed by powder XRD followed by quantitative phase analysis using a whole-pattern-fitting procedure (Rietveld refinement) was determined to be  $66.4 \pm 0.9$  percent amorphous,  $23.5 \pm 0.7$  percent Ca<sub>2</sub>Mg<sub>0.46</sub>Al<sub>0.99</sub>Si<sub>1.52</sub>O<sub>7</sub> (PDF card 98-000-9495),  $6.6 \pm 0.4$  percent CaSiO<sub>4</sub> (PDF card 04-016-5334), and  $3.5 \pm 0.1$  percent SiO<sub>2</sub> (PDF card 00-046-1045).

TABLE I.—CHEMICAL COMPOSITION OF SINTERED HOLLOW-TUBE SAMPLES MEASURED BY ENERGY DISPERSIVE X-RAY SPECTROSCOPY

Sample (nominal composition)	Content, <sup>a,b</sup> mol%								
	HfO <sub>2</sub>	ZrO <sub>2</sub>	Y <sub>2</sub> O <sub>3</sub>	Yb <sub>2</sub> O <sub>3</sub>	Gd <sub>2</sub> O <sub>3</sub>	Nd <sub>2</sub> O <sub>3</sub>	Sc <sub>2</sub> O <sub>3</sub>	Sm <sub>2</sub> O <sub>3</sub>	Dy <sub>2</sub> O <sub>3</sub>
I: ZrO <sub>2</sub> -12Y <sub>2</sub> O <sub>3</sub>	-----	87(3)	12.9(4)	-----	-----	-----	-----	-----	-----
II: ZrO <sub>2</sub> -30Y <sub>2</sub> O <sub>3</sub>	-----	69(2)	30.6(9)	-----	-----	-----	-----	-----	-----
III: HfO <sub>2</sub> -7Dy <sub>2</sub> O <sub>3</sub>	93(3)	-----	-----	-----	-----	-----	-----	-----	6.7(2)
IV: ZrO <sub>2</sub> -9Y <sub>2</sub> O <sub>3</sub> -4.5Gd <sub>2</sub> O <sub>3</sub> -4.5Yb <sub>2</sub> O <sub>3</sub>	-----	84(3)	10.0(3)	2.62(8)	3.3(1)	-----	-----	-----	-----
V: ZrO <sub>2</sub> -9.5Y <sub>2</sub> O <sub>3</sub> -2.25Gd <sub>2</sub> O <sub>3</sub> -2.25Yb <sub>2</sub> O <sub>3</sub>	-----	77(2)	16.0(5)	2.9(1)	4.4(1)	-----	-----	-----	-----
VI: ZrO <sub>2</sub> -3Y <sub>2</sub> O <sub>3</sub> -5Sm <sub>2</sub> O <sub>3</sub> -1.5Yb <sub>2</sub> O <sub>3</sub>	-----	94(3)	4.0(1)	1.18(4)	-----	-----	-----	1.12(3)	-----
VII: ZrO <sub>2</sub> -3Y <sub>2</sub> O <sub>3</sub> -1.5Nd <sub>2</sub> O <sub>3</sub> -1.5Yb <sub>2</sub> O <sub>3</sub> -0.3Sc <sub>2</sub> O <sub>3</sub>	-----	92(3)	4.5(1)	1.63(5)	-----	1.26(4)	0.78(2)	-----	-----

<sup>a</sup>Derived formulas from measured contents of oxides are

I: Zr<sub>0.77±0.03</sub>Y<sub>0.228±0.009</sub>O<sub>2.00±0.06</sub>

II: Zr<sub>0.53±0.02</sub>Y<sub>0.47±0.02</sub>O<sub>2.00±0.05</sub>

III: Hf<sub>0.88±0.04</sub>Dy<sub>0.125±0.005</sub>O<sub>2.00±0.07</sub>

IV: Zr<sub>0.73±0.03</sub>Y<sub>0.172±0.006</sub>Gd<sub>0.056±0.002</sub>Yb<sub>0.045±0.002</sub>O<sub>2.00±0.06</sub>

V: Zr<sub>0.62±0.02</sub>Y<sub>0.259±0.009</sub>Gd<sub>0.07±0.003</sub>Yb<sub>0.046±0.002</sub>O<sub>2.00±0.05</sub>

VI: Zr<sub>0.88±0.04</sub>Y<sub>0.076±0.003</sub>Sm<sub>0.021±0.001</sub>Yb<sub>0.022±0.001</sub>O<sub>2.00±0.07</sub>

VII: Zr<sub>0.85±0.03</sub>Y<sub>0.084±0.003</sub>Nd<sub>0.023±0.001</sub>Yb<sub>0.030±0.001</sub>Sc<sub>0.014±0.001</sub>O<sub>2.00±0.05</sub>

<sup>b</sup>Uncertainties calculated as two standard deviations of the mean are given in parentheses.

TABLE II.—INITIAL PARAMETERS OF SINTERED HOLLOW-TUBE SAMPLES

Sample <sup>a</sup>	CMAS surface concentration, <sup>b</sup> g/cm <sup>2</sup>	BET specific surface area, <sup>c</sup> m <sup>2</sup> /g	Surface area of pores, <sup>d</sup> m <sup>2</sup> /g	Total pore volume ×10 <sup>-5</sup> , cm <sup>3</sup> /g	Density, g/cm <sup>3</sup>	
					Geometric <sup>e</sup>	He pycnometry
I: ZrO <sub>2</sub> -12Y <sub>2</sub> O <sub>3</sub>	147±4	0.0384±0.004	0.024±0.002	3.6±0.4	5.134±0.003	5.72±0.04
II: ZrO <sub>2</sub> -30Y <sub>2</sub> O <sub>3</sub>	69±2	0.307±0.03	0.11±0.01	28±3	5.133±0.03	5.7±0.2
III: HfO <sub>2</sub> -7Dy <sub>2</sub> O <sub>3</sub>	135±4	<0.01	0.07±0.01	14±1	8.23±0.02	9.3±0.2
IV: ZrO <sub>2</sub> -9.0Y <sub>2</sub> O <sub>3</sub> - 4.5Gd <sub>2</sub> O <sub>3</sub> -4.5Yb <sub>2</sub> O <sub>3</sub>	142±4	0.12±0.01	0.036±0.004	12±1	6.186±0.003	6.19±0.09
V: ZrO <sub>2</sub> -9.5Y <sub>2</sub> O <sub>3</sub> - 2.25Gd <sub>2</sub> O <sub>3</sub> -2.25Yb <sub>2</sub> O <sub>3</sub>	104±3	0.12±0.01	0.013±0.001	13±1	6.071±0.003	6.0±0.1
VI: ZrO <sub>2</sub> -3Y <sub>2</sub> O <sub>3</sub> - 1.5Sm <sub>2</sub> O <sub>3</sub> -1.5Yb <sub>2</sub> O <sub>3</sub>	89±3	<0.01	0.16±0.02	30±3	5.8±0.2	5.9±0.1
VII: ZrO <sub>2</sub> -3Y <sub>2</sub> O <sub>3</sub> - 1.5Nd <sub>2</sub> O <sub>3</sub> -1.5Yb <sub>2</sub> O <sub>3</sub> - 0.3Sc <sub>2</sub> O <sub>3</sub>	91±3	<0.01	0.0010±0.0001	3.0±0.3	5.3±0.2	5.9±0.2

<sup>a</sup>Composition of the samples given in mol%.

<sup>b</sup>Calcium-magnesium-aluminum-silicate (CMAS).

<sup>c</sup>Brunauer-Emmett-Teller (BET).

<sup>d</sup>Cumulative measured by BJH (Barrett-Joyner-Halenda) method for pores between 8.5 Å and 150 µm.

<sup>e</sup>Measured in optical microscope.

TABLE III.—COMPARISON OF TARGETED NASA CALCIUM-MAGNESIUM-ALUMINUM-SILICATE (CMAS) COMPOSITIONS MEASURED BY INDUCTIVELY COUPLED PLASMA OPTICAL EMISSION SPECTROSCOPY (ICP-OES) AND ENERGY DISPERSIVE X-RAY SPECTROSCOPY (EDS)

Method	Content, mol%					
	CaO	MgO	Al <sub>2</sub> O <sub>3</sub>	SiO <sub>2</sub>	Fe <sub>2</sub> O <sub>3</sub>	NiO
ICP-OES	30±2	5.3±0.3	11.9±0.6	42±2	8.7±0.4	1.5±0.1
EDS	29.8±0.2	5.9±0.4	13.8±0.5	41.5±0.9	8.0±0.5	1.0±0.4

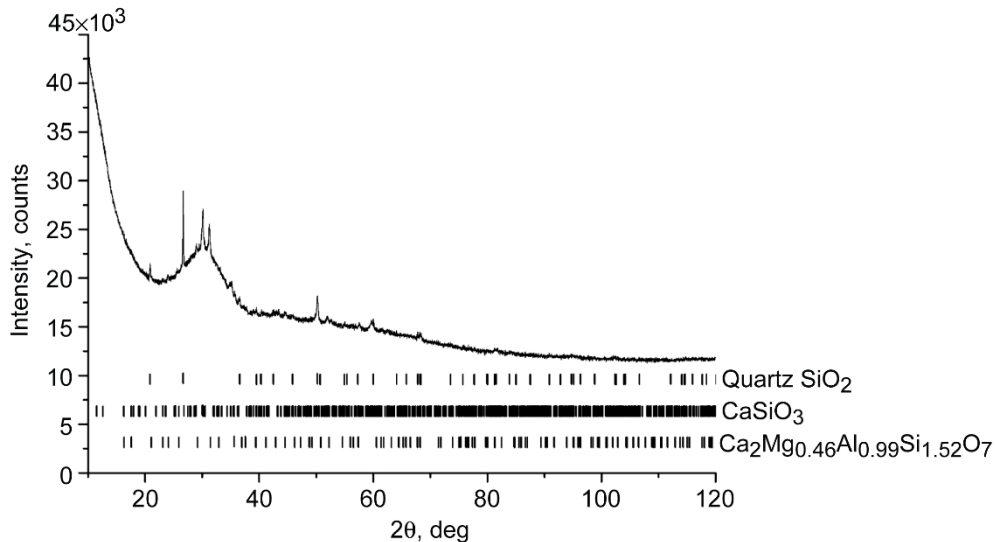


Figure 1.—X-ray diffraction patterns of as-received calcium-magnesium-aluminum-silicate (CMAS) sample.



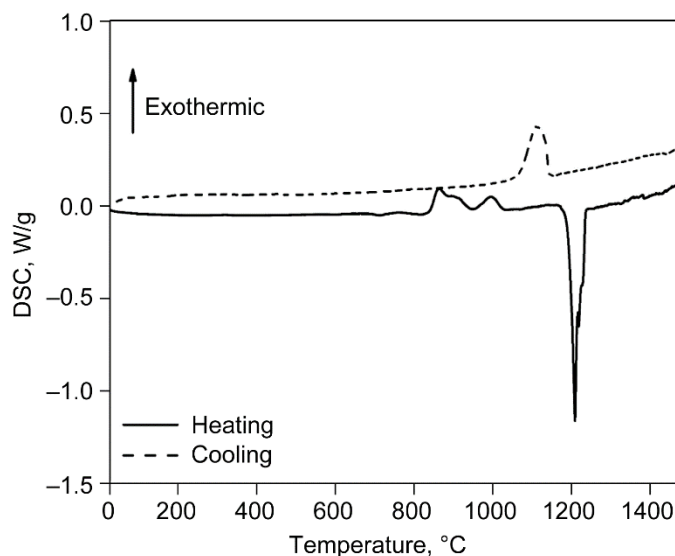


Figure 2.—Differential scanning calorimetry (DSC) traces of calcium-magnesium-aluminum-silicate (CMAS) during heating (solid line) up to 1500 °C at 5 °C/min and then cooling (dashed line).

Figure 2 shows the DSC traces of the NASA CMAS during heating up to 1500 °C (at 5 °C/min) and cooling to room temperature. Four heat effects were observed on heating of the sample to 1500 °C. The first weak endothermic peak, with onset temperature at 692 °C, corresponds to glass transition ( $T_g$ ) of the sample. The weak  $T_g$  endothermic peak is followed by two exothermic peaks, with onset temperatures at 856 and 965 °C, that are related to crystallization of the glass phase. The strongest endothermic peak, related to melting of the NASA CMAS sample, is observed at 1195 °C (onset temperature). During cooling from 1500 °C to room temperature, only an exothermic peak with onset temperature at 1144 °C is observed in the DSC trace. This exothermic peak during cooling corresponds to crystallization of the melted sample. The four heat effects observed in this thermal study corroborates well with those from a previous study (Ref. 16) detected in a differential thermal analysis (DTA) instrument up to 1500 °C at a heating rate of 5 °C/min for a CMAS sample having a different composition (34 wt% SiO<sub>2</sub>, 30 wt% CaSO<sub>4</sub>·2H<sub>2</sub>O, 17 wt% SiO<sub>2</sub>+KAlSi<sub>3</sub>O<sub>8</sub>, 14 wt% dolomite CaMg(CO<sub>3</sub>)<sub>2</sub>, and 5 wt% NaCl).

Figure 3 shows the DSC traces of the NASA CMAS mixed with the 30% YSZ powder coating during heating up to 1500 °C. In addition to the four heat effects related to the NASA CMAS sample (Fig. 2), an endothermic peak with onset temperature at 1258 °C is observed in the DSC trace. This endothermic peak corresponds to the reaction between the NASA CMAS and 30YSZ samples.

SEM images at lower magnification (30× to 80×) of cross sections of the lower cut sections of the hollow-tube samples reacted with CMAS at 1310 °C for 5 h are shown in Figure 4. Note that because of the magnification limits of the SEM instrument, only part of the cross-sectional areas of the hollow tubes were imaged. CMAS reacted and penetrated the inner and outer walls of the platinum-foil-wrapped hollow-tube material, causing an expansion of their volume. Voids or pockets formed after the reaction of the samples and CMAS. The HfO<sub>2</sub>-7Dy<sub>2</sub>O<sub>3</sub> (7DySH) sample III exhibited the lowest CMAS penetration, or highest resistance to CMAS, followed by samples V (ZrO<sub>2</sub>-9.5Y<sub>2</sub>O<sub>3</sub>-2.25Gd<sub>2</sub>O<sub>3</sub>-2.25Yb<sub>2</sub>O<sub>3</sub>) and II (30YSZ). The 25-μm layer observed on the outer wall of the hollow tube is the platinum foil used to wrap and seal the hollow tubes containing CMAS.

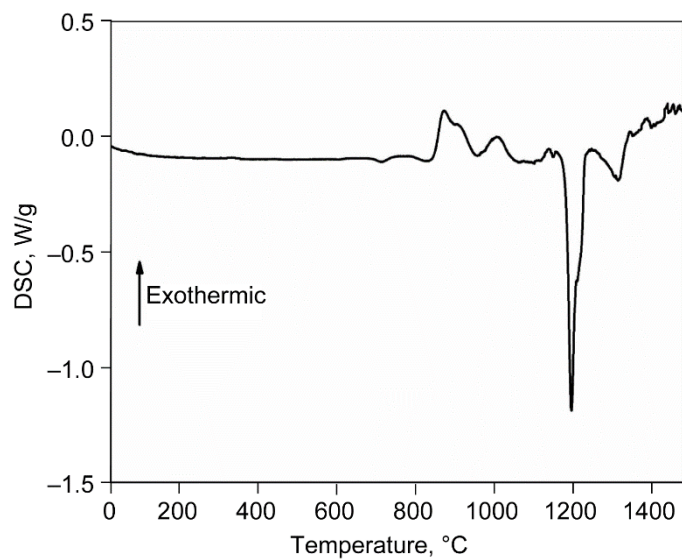


Figure 3.—Differential scanning calorimetry (DSC) traces of calcium-magnesium-aluminum-silicate (CMAS) mixed with sample II  $\text{ZrO}_2\text{-}30\text{Y}_2\text{O}_3$  (1:2 weight ratio) during heating up to 1500 °C at 5 °C/min.

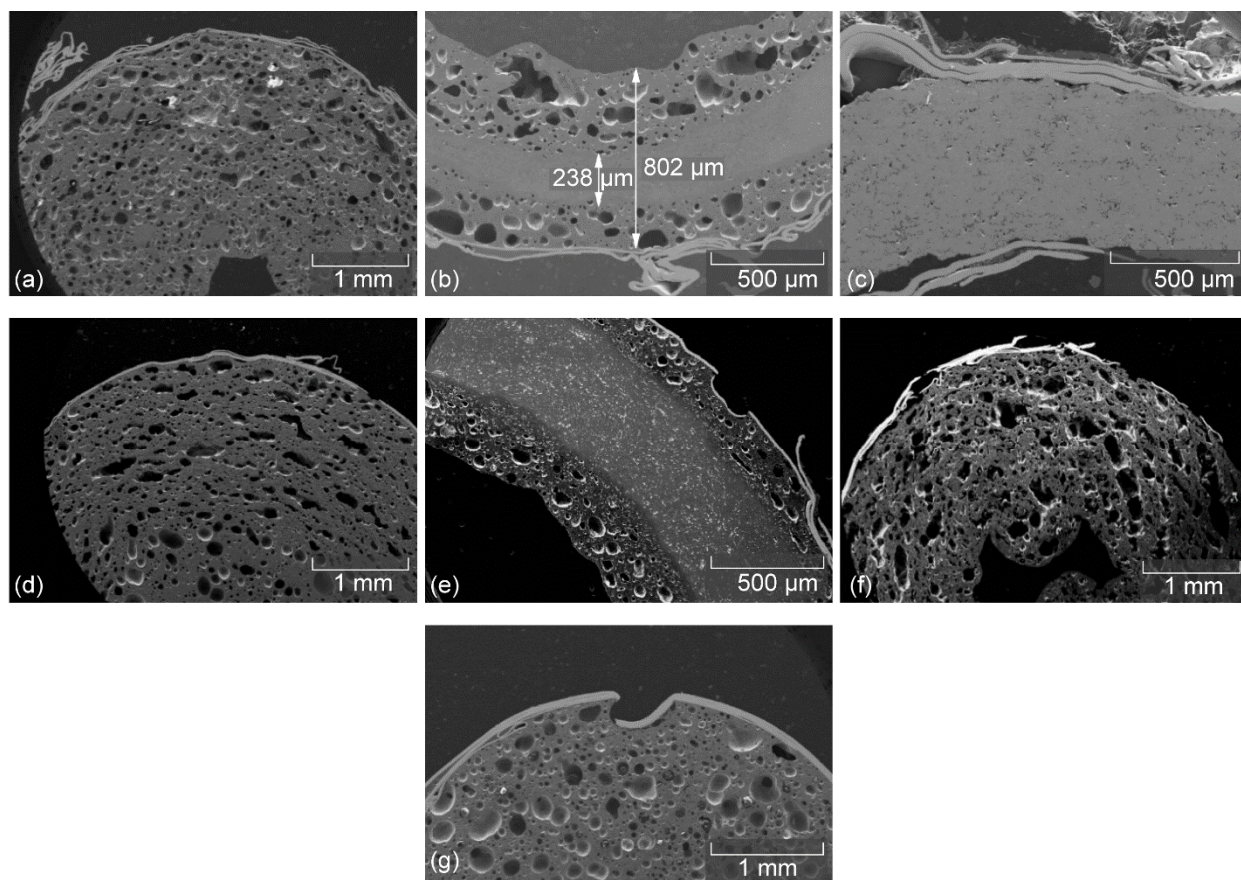


Figure 4.—Scanning electron microscopy images at low magnification of lower section of cross sections of ceramic hollow-tube samples reacted with calcium-magnesium-aluminum-silicate (CMAS) at 1310 °C for 5 h. (a) I:  $\text{ZrO}_2\text{-}12\text{Y}_2\text{O}_3$ . (b) II:  $\text{ZrO}_2\text{-}30\text{Y}_2\text{O}_3$ . (c) III:  $\text{HfO}_2\text{-}7\text{Dy}_2\text{O}_3$ . (d) IV:  $\text{ZrO}_2\text{-}9.0\text{Y}_2\text{O}_3\text{-}4.5\text{Gd}_2\text{O}_3\text{-}4.5\text{Yb}_2\text{O}_3$ . (e) V:  $\text{ZrO}_2\text{-}9.5\text{Y}_2\text{O}_3\text{-}2.25\text{Gd}_2\text{O}_3\text{-}2.25\text{Yb}_2\text{O}_3$ . (f) VI:  $\text{ZrO}_2\text{-}3.0\text{Y}_2\text{O}_3\text{-}1.5\text{Sm}_2\text{O}_3\text{-}1.5\text{Yb}_2\text{O}_3$ . (g) VII:  $\text{ZrO}_2\text{-}3.0\text{Y}_2\text{O}_3\text{-}1.5\text{Nd}_2\text{O}_3\text{-}1.5\text{Yb}_2\text{O}_3\text{-}0.3\text{Sc}_2\text{O}_3$ .

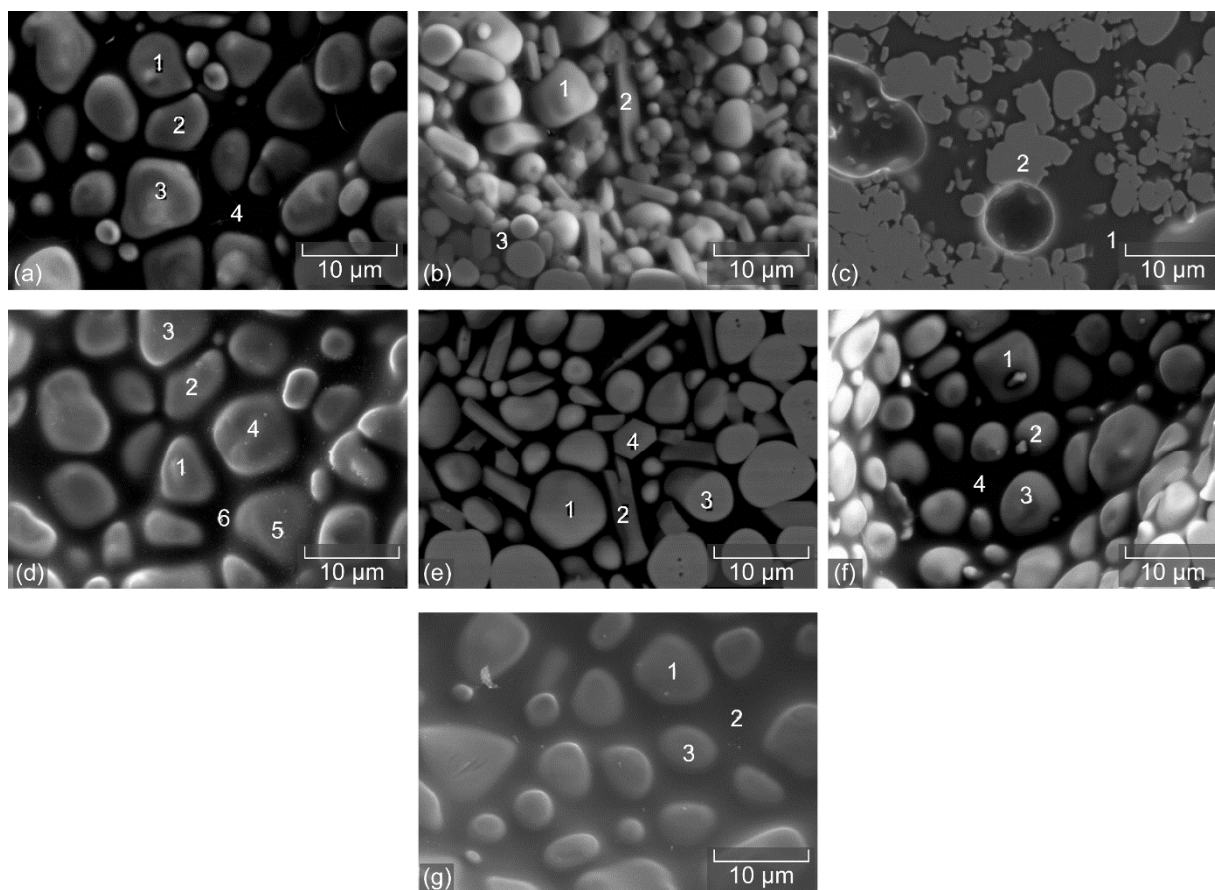


Figure 5.—Scanning electron microscopy images at high magnification (3000×) of lower section of cross sections of ceramic hollow-tube samples reacted with calcium-magnesium-aluminum-silicate (CMAS) at 1310 °C for 5 h. (a) I:  $\text{ZrO}_2\text{-12Y}_2\text{O}_3$ . (b) II:  $\text{ZrO}_2\text{-30Y}_2\text{O}_3$ . (c) III:  $\text{HfO}_2\text{-7Dy}_2\text{O}_3$ . (d) IV:  $\text{ZrO}_2\text{-9.0Y}_2\text{O}_3\text{-4.5Gd}_2\text{O}_3\text{-4.5Yb}_2\text{O}_3$ . (e) V:  $\text{ZrO}_2\text{-9.5Y}_2\text{O}_3\text{-2.25Gd}_2\text{O}_3\text{-2.25Yb}_2\text{O}_3$ . (f) VI:  $\text{ZrO}_2\text{-3.0Y}_2\text{O}_3\text{-1.5Sm}_2\text{O}_3\text{-1.5Yb}_2\text{O}_3$ . (g) VII:  $\text{ZrO}_2\text{-3.0Y}_2\text{O}_3\text{-1.5Nd}_2\text{O}_3\text{-1.5Yb}_2\text{O}_3\text{-0.3Sc}_2\text{O}_3$ .

SEM images at higher magnification (3000×) of the hollow-tube sample cross sections reacted with NASA CMAS at 1310 °C for 5 h are shown in Figure 5. The areas imaged are near to the inner edge of the hollow-tube walls and are referred to here as “reacted regions.” CMAS melted, reacted, or penetrated the coating material through the grain boundaries as seen in the dark areas of the electron micrographs. Sample V  $\text{ZrO}_2\text{-9.5Y}_2\text{O}_3\text{-2.25Gd}_2\text{O}_3\text{-2.25Yb}_2\text{O}_3$  is the only one that the (dark area) grain boundary is not evident from the image at 3000× magnification. The grains in the samples with total rare earth ( $\text{RE}_2\text{O}_3$ ) content up to 12 mol% are approximately of the same shape and have their boundaries rounded, with possible exception of the  $\text{HfO}_2$  coating. Samples with total  $\text{RE}_2\text{O}_3$  content higher than 12 mol% exhibited rectangular-shaped grains in addition to the rounded grains in their microstructure.

Chemical composition of the samples measured by EDS analysis are given in Table IV. The grain boundaries of the reacted samples I to IV, VI, and VII are rich in  $\text{SiO}_2$  (33 to 51 mol%) and  $\text{CaO}$  (25 to 48 mol%) with minor amounts of  $\text{ZrO}_2$  (2 to 20 mol%) for the zirconia-based samples I and IV to VII;  $\text{HfO}_2$  (0.8 mol%) for the hafnia sample; RE oxides (0.9 to 4 mol%, total);  $\text{MgO}$  (6 to 11 mol%); and  $\text{Al}_2\text{O}_3$  (2 to 9 mol%). In addition to the major components of CMAS detected by EDS in the grain boundary of the reacted samples, 2 to 5 mol%  $\text{Fe}_2\text{O}_3$  was detected in samples I, III, IV, VI, and VII, and 1 mol%  $\text{NiO}$  was detected in samples I and IV. EDS analysis detected high contents of  $\text{SiO}_2$  (43 mol%),  $\text{CaO}$  (16 mol%), and  $\text{Y}_2\text{O}_3$  (22 mol%) in grains 2 and 4 of sample V (Fig. 5). Note the grain boundary is not observed in the SEM image of this sample (Fig. 5). In addition to the CMAS-rich components detected in the grain boundaries of samples II and IV, EDS analysis also detected high contents of  $\text{CaO}$

(21 mol%), SiO<sub>2</sub> (43 mol%), and Y<sub>2</sub>O<sub>3</sub> (31 mol%) in grain 2 of sample II as well as high contents of CaO (11 mol%) and SiO<sub>2</sub> (43 mol%) and a low content of Y<sub>2</sub>O<sub>3</sub> (2 mol%) in grains 1 to 3 of sample IV. In general, the grains of the reacted samples that retained most of their initial composition still exhibited minor amounts of SiO<sub>2</sub> (2 to 4 mol%), CaO (3 to 6 mol%), MgO (0 to 1 mol%), Al<sub>2</sub>O<sub>3</sub> (0.2 to 0.5 mol%), and Fe<sub>2</sub>O<sub>3</sub> (0.5 to 2 mol%).

The XRD pattern of the lower section of hollow-tube samples reacted with CMAS are presented in Figures 6 to 12. Fluorite or cubic symmetry (PDF card 01-077-2115) was detected by XRD analysis as the main crystalline phase in the zirconia-based samples with initial RE content higher than 12 mol%. Beyond the cubic phase, hexagonal or oxyapatite silicate secondary phases Ca<sub>4</sub>Y<sub>6</sub>O(SiO<sub>4</sub>)<sub>6</sub> (PDF card 00-027-0093) and CaY<sub>4</sub>(SiO<sub>4</sub>)<sub>3</sub>O (PDF card 04-007-9210) were detected by XRD in samples IV ZrO<sub>2</sub>-9Y<sub>2</sub>O<sub>3</sub>-4.5Gd<sub>2</sub>O<sub>3</sub>-4.5Yb<sub>2</sub>O<sub>3</sub> and V ZrO<sub>2</sub>-9.5Y<sub>2</sub>O<sub>3</sub>-2.25Gd<sub>2</sub>O<sub>3</sub>-2.25Yb<sub>2</sub>O<sub>3</sub>, respectively. Hexagonal Zr<sub>3</sub>Yb<sub>4</sub>O<sub>12</sub> (PDF card 04-002-0210) secondary phase was also detected in sample V ZrO<sub>2</sub>-9.5Y<sub>2</sub>O<sub>3</sub>-2.25Gd<sub>2</sub>O<sub>3</sub>-2.25Yb<sub>2</sub>O<sub>3</sub>. There were three different secondary phases (hexagonal Ca<sub>4</sub>Y<sub>6</sub>O(SiO<sub>4</sub>)<sub>6</sub>, PDF card 00-027-0093; hexagonal CaY<sub>4</sub>(SiO<sub>4</sub>)<sub>3</sub>O, PDF card 04-007-9210; and cubic Mg<sub>5</sub>Y<sub>6</sub>Si<sub>5</sub>O<sub>24</sub>, PDF card 00-020-0696) detected by XRD in sample II 30YSZ. XRD only detected tetragonal crystalline phases in zirconia-based samples VI ZrO<sub>2</sub>-3Y<sub>2</sub>O<sub>3</sub>-1.5Sm<sub>2</sub>O<sub>3</sub>-1.5Yb<sub>2</sub>O<sub>3</sub> and VII ZrO<sub>2</sub>-3Y<sub>2</sub>O<sub>3</sub>-1.5Nd<sub>2</sub>O<sub>3</sub>-1.5Yb<sub>2</sub>O<sub>3</sub>-0.3Sc<sub>2</sub>O<sub>3</sub>. Cubic (PDF card 04-005-6040) and monoclinic (PDF card 98-001-7637) phases were detected in the reacted hafnia-based sample HfO<sub>2</sub>-7Dy<sub>2</sub>O<sub>3</sub>.

TABLE IV.—COMPOSITION OF LOWER SECTION OF HOLLOW-TUBE SAMPLES REACTED WITH  
CALCIUM-MAGNESIUM-ALUMINUM-SILICATE (CMAS) ANALYZED BY ELECTRON DISPERSION SPECTROSCOPY

Sample <sup>a</sup>	Content, <sup>b</sup> mol%														
	HfO <sub>2</sub>	ZrO <sub>2</sub>	Y <sub>2</sub> O <sub>3</sub>	Yb <sub>2</sub> O <sub>3</sub>	Gd <sub>2</sub> O <sub>3</sub>	Nd <sub>2</sub> O <sub>3</sub>	Sc <sub>2</sub> O <sub>3</sub>	Sm <sub>2</sub> O <sub>3</sub>	Dy <sub>2</sub> O <sub>3</sub>	CaO	MgO	NiO	SiO <sub>2</sub>	Al <sub>2</sub> O <sub>3</sub>	Fe <sub>2</sub> O <sub>3</sub>
I	-----	81(1)	11.9(2)	-----	-----	-----	-----	-----	-----	2.8(2)	1.2(3)	-----	2.0(2)	0.4(1)	0.6(1)
	-----	20.0(4)	4.4(2)	-----	-----	-----	-----	-----	-----	24.7(4)	6.6(3)	1.0(3)	35.2(6)	5.7(1)	2.4(1)
II	-----	75(2)	18.8(5)	-----	-----	-----	-----	-----	-----	3(2)	1.2(2)	-----	1.4(2)	0.4(1)	-----
	-----	3.3(2)	31.1(3)	-----	-----	-----	-----	-----	-----	21.3(2)	1.1(2)	-----	42.5(4)	0.66(9)	-----
	-----	4.8(2)	4.2(1)	-----	-----	-----	-----	-----	-----	47.5(4)	8.8(2)	-----	32.7(4)	1.9(1)	-----
III	85(5)	-----	-----	-----	-----	-----	-----	-----	6.9(8)	-----	6.0(6)	-----	-----	1.2(3)	0.8(4)
	0.8(5)	-----	-----	-----	-----	-----	-----	-----	1.3(2)	25.3(6)	11.2(6)	-----	51(1)	8.9(4)	2.0(2)
IV	-----	52(1)	1.7(6)	7.4(2)	3.1(1)	-----	-----	-----	-----	11.2(9)	3.4(9)	-----	17(1)	3.5(5)	1.4(4)
	-----	77.6(9)	3.2(3)	4.4(2)	2.4(1)	-----	-----	-----	-----	5.8(4)	1.1(4)	-----	4.1(3)	0.5(2)	1.8(4)
	-----	7.7(4)	0.6(2)	2.23(3)	1.4(2)	-----	-----	-----	-----	32.1(6)	6.3(3)	-----	38.4(8)	6.3(1)	4.9(2)
V	-----	79(1)	10.3(2)	3.7(3)	3.0(2)	-----	-----	-----	-----	2.7(3)	-----	-----	0.8(2)	0.23(8)	-----
	-----	5.4(3)	21.5(4)	3.5(3)	10.4(3)	-----	-----	-----	-----	15.8(3)	-----	-----	42.5(5)	0.8(2)	-----
VI	-----	86.4(8)	2.6(1)	1.4(2)	-----	-----	-----	1.1(1)	-----	4.1(2)	1.4(2)	-----	3.5(2)	0.24(9)	0.50(8)
	-----	9.4(3)	0.34(9)	0.6(1)	-----	-----	-----	1.1(1)	-----	27.0(3)	6.9(3)	1.2(2)	43.7(5)	6.8(1)	2.9(1)
VII	-----	87(2)	1.5(2)	1.4(5)	-----	1.8(6)	0.2(1)	-----	-----	4.5(4)	1.4(5)	-----	1.4(4)	-----	0.9(2)
	-----	2.2(3)	0.2(2)	1.0(3)	-----	2.3(4)	-----	-----	-----	28.2(6)	8.8(5)	-----	47.3(8)	7.5(3)	2.6(2)

<sup>a</sup>I: ZrO<sub>2</sub>-12Y<sub>2</sub>O<sub>3</sub> (see Fig. 5(a))

II: ZrO<sub>2</sub>-30Y<sub>2</sub>O<sub>3</sub> (see Fig. 5(b))

III: HfO<sub>2</sub>-7Dy<sub>2</sub>O<sub>3</sub> (see Fig. 5(c))

IV: ZrO<sub>2</sub>-9Y<sub>2</sub>O<sub>3</sub>-4.5Gd<sub>2</sub>O<sub>3</sub>-4.5Yb<sub>2</sub>O<sub>3</sub> (see Fig. 5(d))

V: ZrO<sub>2</sub>-9.5Y<sub>2</sub>O<sub>3</sub>-2.25Gd<sub>2</sub>O<sub>3</sub>-2.25Yb<sub>2</sub>O<sub>3</sub> (see Fig. 5(e))

VI: ZrO<sub>2</sub>-3Y<sub>2</sub>O<sub>3</sub>-1.5Sm<sub>2</sub>O<sub>3</sub>-1.5Yb<sub>2</sub>O<sub>3</sub> (see Fig. 5(f))

VII: ZrO<sub>2</sub>-3Y<sub>2</sub>O<sub>3</sub>-1.5Nd<sub>2</sub>O<sub>3</sub>-1.5Yb<sub>2</sub>O<sub>3</sub>-0.3Sc<sub>2</sub>O<sub>3</sub> (see Fig. 5(g))

G is grain, and GB is grain boundary.

<sup>b</sup>Uncertainties calculated as two standard deviations of the mean are given in parentheses.

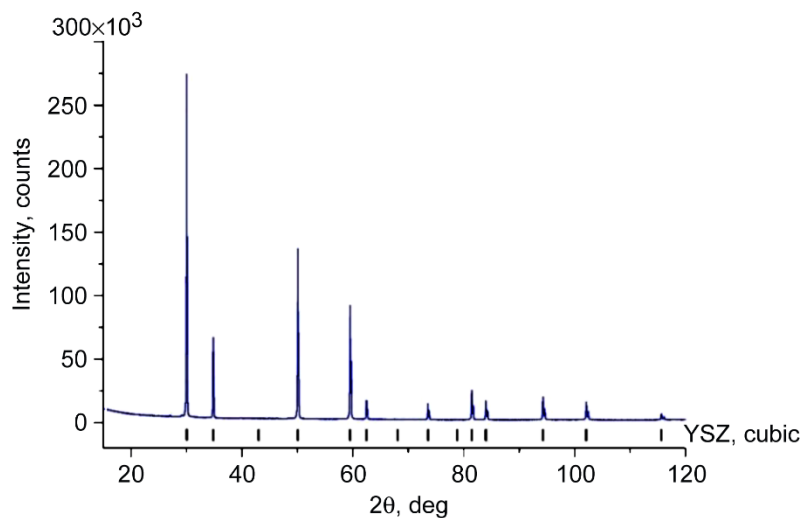


Figure 6.—X-ray diffraction pattern of ground lower section of 12% yttria-stabilized zirconia (YSZ) hollow-tube sample I reacted with calcium-magnesium-aluminum-silicate (CMAS).

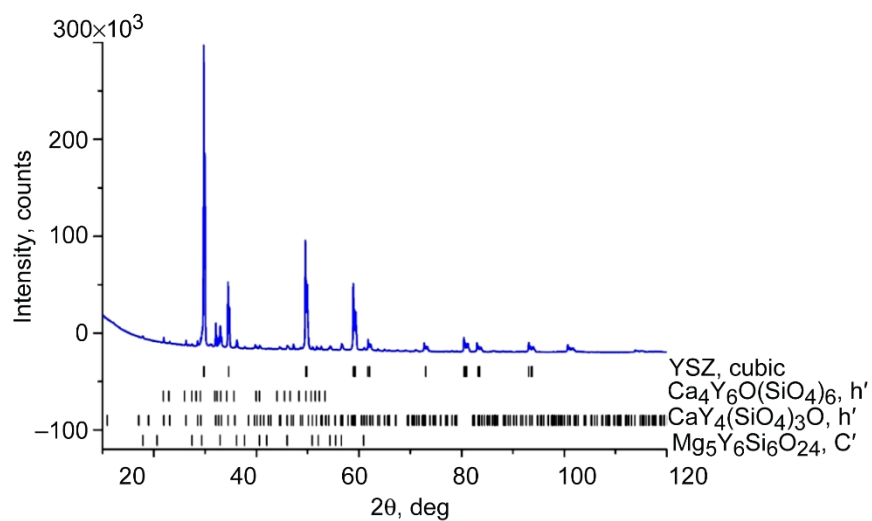


Figure 7.—X-ray diffraction pattern of ground lower section of 30% yttria-stabilized zirconia (YSZ) hollow-tube sample II reacted with calcium-magnesium-aluminum-silicate (CMAS).

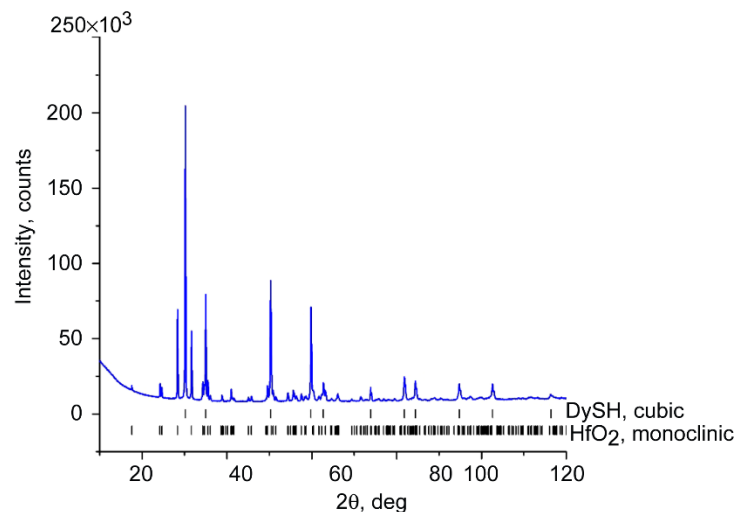


Figure 8.—X-ray diffraction pattern of ground lower section of  $\text{HfO}_2\text{-7Dy}_2\text{O}_3$  (7DySH) hollow-tube sample III reacted with calcium-magnesium-aluminum-silicate (CMAS).

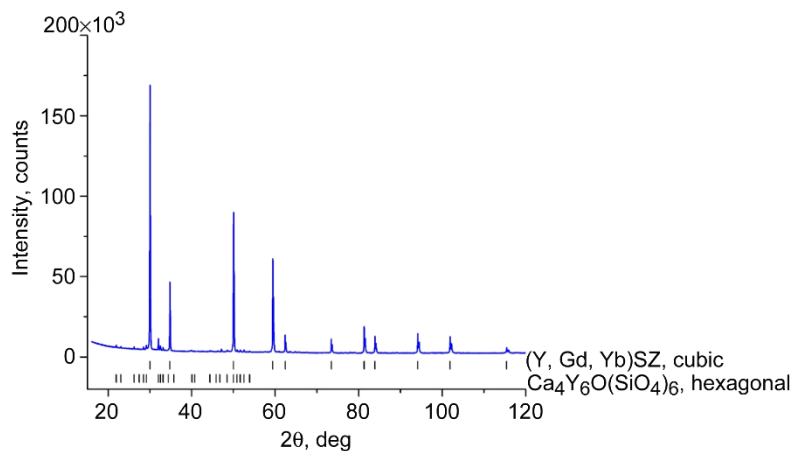


Figure 9.—X-ray diffraction pattern of ground lower section of  $\text{ZrO}_2\text{-9.0Y}_2\text{O}_3\text{-4.5Gd}_2\text{O}_3\text{-4.5Yb}_2\text{O}_3$  hollow-tube sample IV reacted with calcium-magnesium-aluminum-silicate (CMAS).

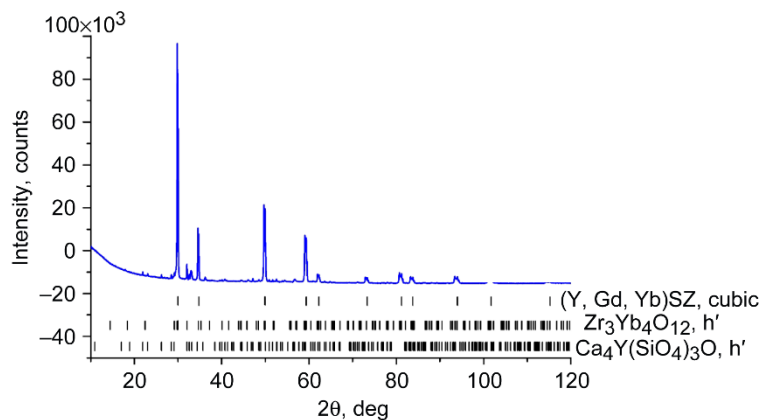


Figure 10.—X-ray diffraction pattern of ground lower section of  $\text{ZrO}_2\text{-9.5Y}_2\text{O}_3\text{-2.25Gd}_2\text{O}_3\text{-2.25Yb}_2\text{O}_3$  hollow-tube sample V reacted with calcium-magnesium-aluminum-silicate (CMAS).



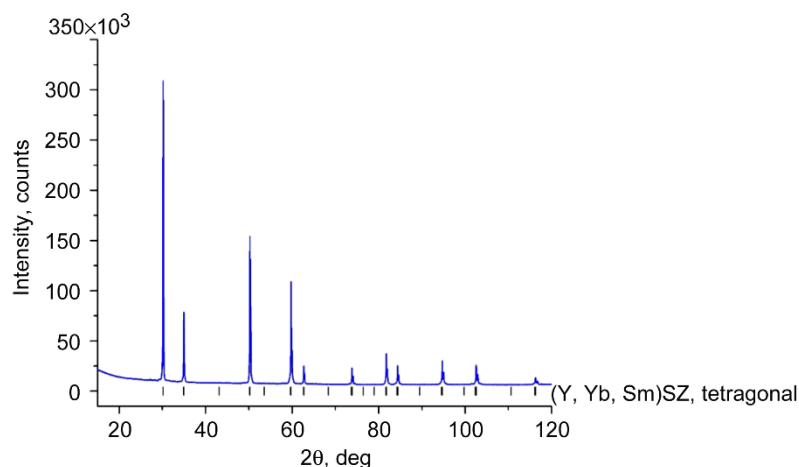


Figure 11.—X-ray diffraction pattern of ground lower section of  $\text{ZrO}_2$ - $3.0\text{Y}_2\text{O}_3$ - $1.5\text{Sm}_2\text{O}_3$ - $1.5\text{Yb}_2\text{O}_3$  hollow-tube sample VI reacted with calcium-magnesium-aluminum-silicate (CMAS).

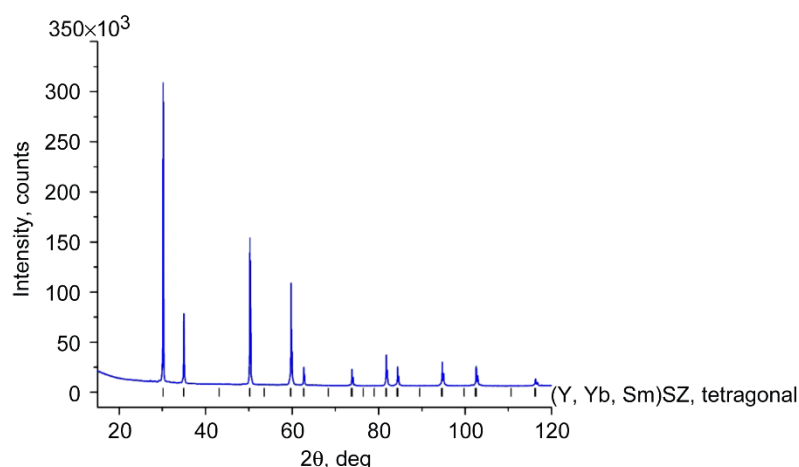


Figure 12.—X-ray diffraction pattern of ground lower section of  $\text{ZrO}_2$ - $3.0\text{Y}_2\text{O}_3$ - $1.5\text{Nd}_2\text{O}_3$ - $1.5\text{Yb}_2\text{O}_3$ - $0.3\text{Sc}_2\text{O}_3$  hollow-tube sample VII reacted with calcium-magnesium-aluminum-silicate (CMAS).

## Discussion

CMAS first melted before it penetrated or reacted with the samples at the grain boundaries via melt/solid-state diffusion, forming a CMAS compound containing the REs, zirconium, or hafnium. The products of the reaction or phases detected in this work and the penetration mechanisms of CMAS corroborates well with those found by Ahlborg and Zhu (Ref. 17) in the  $\text{HfO}_2$ -23.9 mol% (Gd, Yb, Y) $_2\text{O}_3$  and  $\text{ZrO}_2$ -4.4 mol% (Y, Gd, Yb) $_2\text{O}_3$ -2.6 mol% ( $\text{TiO}_2 + \text{Ta}_2\text{O}_5$ ) compositions reacted with CMAS (35 mol% CaO-10 mol% MgO-7 mol%  $\text{Al}_2\text{O}_3$ -48 mol%  $\text{SiO}_2$  with minor amounts of  $\text{Fe}_2\text{O}_3$  and NiO, provided by General Electric) at 1500 °C for 100 h. In this work, EDS analysis detected high contents of silicon and oxygen in the grain boundaries of the samples with a total amount of REs up to 12 mol%. Note that no silicate phase was detected by XRD in these samples implying that its content was below the detection limit of the XRD instrument or that the silicate phase is amorphous. Above 12 mol% REs, this silicate compound or phase may have crystallized into oxyapatite phases ( $\text{Ca}_4\text{Y}_6\text{O}(\text{SiO}_4)_6$  and  $\text{CaY}_4(\text{SiO}_4)_3\text{O}$  as evident from the XRD, depending on the sample), which were formed only in the samples with a total amount of REs higher than 12 mol%. Note that some elemental substitutions are possible in the structural sites of the phases; for example, calcium can be replaced by magnesium, and yttrium can be replaced by



aluminum, iron, or other REs. These substitutions are evident in the grains 1, 2, and 3 of sample IV since elements other than calcium, yttrium, and silicon are detected by EDS in this sample.

The fact that the CMAS did not completely penetrate sample V ( $\text{ZrO}_2\text{-}9.5\text{Y}_2\text{O}_3\text{-}2.25\text{Gd}_2\text{O}_3\text{-}2.25\text{Yb}_2\text{O}_3$ ) when compared with sample IV ( $\text{ZrO}_2\text{-}9.0\text{Y}_2\text{O}_3\text{-}4.5\text{Gd}_2\text{O}_3\text{-}4.5\text{Yb}_2\text{O}_3$ ) containing the same elements, but with higher RE content, may be due to possible actual higher  $\text{Y}_2\text{O}_3$  content in the sample, thus leading to higher  $\text{Y}_2\text{O}_3$  in the CMAS melt and helping the complete conversion of CMAS and the sample material to the final products of the reaction or crystalline phases oxyapatite ( $\text{CaY}_4(\text{SiO}_4)_3\text{O}$ ) and  $\text{Zr}_3\text{Yb}_4\text{O}_{12}$ .

Note that sample IV ( $\text{ZrO}_2\text{-}9.0\text{Y}_2\text{O}_3\text{-}4.5\text{Gd}_2\text{O}_3\text{-}4.5\text{Yb}_2\text{O}_3$ ) contained the same elements, but with lower  $\text{Y}_2\text{O}_3$  and higher RE content, and exhibited amorphous and crystalline phases, indicating that reaction reached an equilibrium where the most stable phases formed are cubic zirconia, oxyapatite, and amorphous silicate phases. The higher RE contents of this sample might have led to a RE–CMAS melt composition that does not favor a stability field for the crystalline oxyapatite phases. In contrast, the 30YSZ sample with higher content of  $\text{Y}_2\text{O}_3$  was more resistant (less penetration) to the CMAS melt than the 12YSZ sample with lower yttrium content. For this system containing only zirconia and yttria, the lower  $\text{Y}_2\text{O}_3$  content of the 12YSZ was not enough to react with the CMAS melt to form stable oxyapatite crystalline phases at the temperature of the reaction. From these observations, we conclude that the most resistant samples to CMAS penetration are those in which potentially higher melting glass CMAS forms, or only samples that favor the formation of crystalline phases between the reaction of a vast amount of CMAS material and a minimum amount of RE. Although the relation between the stability field of the competing phases in the system involving the sample and CMAS melt works well to explain our initial findings, further work exploring other parameters as kinetics and the effect of the RE oxide clusters of reduced coating solid diffusivity still need to be done. Based on the current results, the combination of high stability composition cluster oxide coating materials and dopant elements stabilize the CMAS melts and are likely to contribute to a more CMAS-resistant coating system.

The relative stability of zirconia-based samples can be assessed and discussed regarding their resistance to the CMAS melt reaction using the concept of optical basicity of zirconium or the RE oxides (Refs. 12 and 18 to 20). Optical basicity, which is another measure of the basicity of a metal oxide, is a measure of the electron donation capability of the oxygen anion to a particular cation (here,  $\text{Zr}^{4+}$ ,  $\text{Y}^{3+}$ ,  $\text{Gd}^{3+}$ ,  $\text{Nd}^{3+}$ ,  $\text{Sm}^{3+}$ ,  $\text{Sc}^{3+}$ , or  $\text{Yb}^{3+}$ ) (Refs. 18 to 20). Optical basicity generally uses data from X-ray photoelectron (Ref. 21) and ultraviolet (UV) (Ref. 18) spectroscopy data as input parameters. Here the optical basicity of zirconia-based samples is calculated through the following equation (Ref. 18):

$$\Lambda_{\text{th}} = \frac{ax\Lambda_{\text{ZrO}_2} + \left[ by\Lambda_{(\text{RE}_2\text{O}_3)_1} + cz\Lambda_{(\text{RE}_2\text{O}_3)_2+\dots} \right]}{2n} \quad \text{for } \text{Zr}_x^{a+} \left[ (\text{RE}_y^{b+})_1 (\text{RE}_z^{c+})_2 \dots \right] \text{O}_n^{2-} \quad (1)$$

where  $a^+$ ,  $b^+$ , and  $c^+$  are the valences, and  $x$ ,  $y$ ,  $z$ , and  $n$  are the stoichiometric coefficients for  $\text{Zr}^{4+}$ ,  $\text{RE}^{3+}$ , and  $\text{O}^{2-}$ . The stoichiometric coefficients used in these calculations are given in the footnote of Table I. The known optical basicities of zirconia or of the REs are given in Table V.

TABLE V.—OPTICAL BASICITY  
OF ZIRCONIA AND  
RARE EARTH OXIDES

Oxide	Optical basicity, $\Lambda_{\text{th}}$	Reference
$\text{Y}_2\text{O}_3$	1	18
$\text{Yb}_2\text{O}_3$	0.94	22
$\text{Nd}_2\text{O}_3$	1.19	22
$\text{Sm}_2\text{O}_3$	1.14	22
$\text{Gd}_2\text{O}_3$	1.18	22
$\text{Dy}_2\text{O}_3$	1.08	22
$\text{Sc}_2\text{O}_3$	0.89	18
$\text{ZrO}_2$	0.86	23

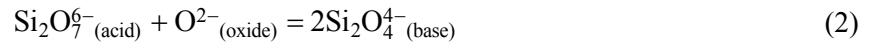
TABLE VI.—THEORETICAL OPTICAL BASICITY  
OF ZIRCONIA-BASED SAMPLES<sup>a</sup>

Sample# (nominal composition)	Optical basicity, $\Lambda_{th}$
I: ZrO <sub>2</sub> -12Y <sub>2</sub> O <sub>3</sub>	0.83
II: ZrO <sub>2</sub> -30Y <sub>2</sub> O <sub>3</sub>	0.81
IV: ZrO <sub>2</sub> -9Y <sub>2</sub> O <sub>3</sub> -4.5Gd <sub>2</sub> O <sub>3</sub> -4.5Yb <sub>2</sub> O <sub>3</sub>	0.84
V: ZrO <sub>2</sub> -9.5Y <sub>2</sub> O <sub>3</sub> -2.25Gd <sub>2</sub> O <sub>3</sub> -2.25Yb <sub>2</sub> O <sub>3</sub>	0.83
VI: ZrO <sub>2</sub> -3Y <sub>2</sub> O <sub>3</sub> -1.5Sm <sub>2</sub> O <sub>3</sub> -1.5Yb <sub>2</sub> O <sub>3</sub>	0.85
VII: ZrO <sub>2</sub> -3Y <sub>2</sub> O <sub>3</sub> -1.5Nd <sub>2</sub> O <sub>3</sub> -1.5Yb <sub>2</sub> O <sub>3</sub> -0.3Sc <sub>2</sub> O <sub>3</sub>	0.84

<sup>a</sup>Calculated with Equation (1) and data of Table V.

The optical basicity obtained by Equation (1) is the mean value of the constituents' metal oxides, accounting for charge neutralization of each cation, and it does not take into account structural parameters. This method is used since there are no data available for the optical basicity of RE<sup>3+</sup> that considers structural parameters (e.g., coordination number and spin state of the cation) and since it has been successfully applied to explain the trend in properties of silicate glasses (Ref. 18), silicate-based coatings (Ref. 24), and framework titanates (Ref. 25). The calculated theoretical optical basicities of the zirconia-based samples are given in Table VI. The optical basicity of the hafnia-based sample was not calculated since the optical basicity of hafnium or hafnium oxide is still not available in the literature.

It is noticed here that the zirconia-based samples II ZrO<sub>2</sub>-30Y<sub>2</sub>O<sub>3</sub> and V ZrO<sub>2</sub>-9.6Y<sub>2</sub>O<sub>3</sub>-2.25Gd<sub>2</sub>O<sub>3</sub>-2.25Yb<sub>2</sub>O<sub>3</sub> with the lowest optical basicity seemed more resistant to CMAS or showed less depth of CMAS melt penetration. It has been proposed by Navrotsky (Refs. 26 and 27) that the acid-base character of oxide melts (e.g., CMAS) is governed by its acid-base equilibrium:



Acid-base interactions, network substitution of silicon and aluminum, and mixing of nonnetwork cations are the main processes occurring when an oxide sample reacts with the silicate (CMAS) melt (Ref. 28). It is likely that the zirconia-based samples having the lowest optical basicity, or being the weakest bases, are less reactive to the silicate oxide melt (CMAS), which have a component with acid character. The better CMAS resistance of ZrO<sub>2</sub>-9.6Y<sub>2</sub>O<sub>3</sub>-2.25Gd<sub>2</sub>O<sub>3</sub>-2.25Yb<sub>2</sub>O<sub>3</sub> than 12YSZ, considering that both have an optical basicity of 0.83, may be related to the higher optical basicity of RE oxides Gd<sub>2</sub>O<sub>3</sub> and Yb<sub>2</sub>O<sub>3</sub>, which would drive Equation (2) more to the right, resulting in a melt with more base character at the grain boundaries of the samples, which ideally diminishes their reactivity with CMAS melt. However, the results are not convincing because of the complexity of the coating systems and the coating-CMAS interactions, particularly when in contact with a large amount of CMAS melts. In general, one can expect that the most CMAS-resistant coating system will be the one with sufficient contents of RE oxides of high optical basicity while also containing highly stable and low-optical-basicity base and RE oxides, effectively stabilizing CMAS and minimizing coating loss to the CMAS melts at high temperatures.

## Conclusions

The thermochemistry reactions and stability of advanced plasma-sprayed ZrO<sub>2</sub>- and HfO<sub>2</sub>-based components of thermal and environmental barrier coatings systems in contact with CMAS have been investigated at 1310 °C. The effects of yttria and rare earth dopants on the coating CMAS resistance have been particularly studied. It has been found that HfO<sub>2</sub>-7Dy<sub>2</sub>O<sub>3</sub>, ZrO<sub>2</sub>-9.6Y<sub>2</sub>O<sub>3</sub>-2.25Gd<sub>2</sub>O<sub>3</sub>-2.25Yb<sub>2</sub>O<sub>3</sub>, and ZrO<sub>2</sub>-30Y<sub>2</sub>O<sub>3</sub> coatings had the highest CMAS stability. The CMAS resistance has been attributed to the incorporation of high optical basicity oxide dopants and also the intrinsic high-stability base and dopant material systems that have low optical basicity, particularly as illustrated in the HfO<sub>2</sub> and multicomponent ZrO<sub>2</sub> cluster coating cases. The multicomponent dopant oxide cluster coatings may have a significant benefit in achieving the overall coating CMAS resistance.

## References

1. Spitsberg, Irene; and Steibel, Jim: Thermal and Environmental Barrier Coatings for SiC/SiC CMCs in Aircraft Engine Applications. *Int. J. Appl. Ceram. Technol.*, vol. 1, no. 4, 2004, pp. 291–301.
2. Padture, Nitin P.: Advanced Structural Ceramics in Aerospace Propulsion. *Nat. Mater.*, vol. 15, 2016, pp. 804–809.
3. Lee, K.N.: Current Status of Environmental Barrier Coatings for Si-Based Ceramics. *Surf. Coat. Technol.*, vol. 133–134, 2000, pp. 1–7.
4. Lee, Kang N., et al.: Upper Temperature Limit of Environmental Barrier Coatings Based on Mullite and BSAS. *J. Am. Ceram. Soc.*, vol. 86, no. 8, 2003, pp. 1299–1306.
5. Lee, Kang N.; Fox, Dennis S.; and Bansal, Narottam P.: Rare Earth Silicate Environmental Barrier Coatings for SiC/SiC Composites and Si<sub>3</sub>N<sub>4</sub> Ceramics. *J. Eur. Ceram. Soc.*, vol. 25, 2005, pp. 1705–1715.
6. Zhu, D.: Advanced Environmental Barrier Coatings for SiC/SiC Ceramic Matrix Composite Turbine Components. *Engineered Ceramics: Current Status and Future Prospects*, T. Ohji and M. Singh, eds., John Wiley & Sons, Hoboken, NJ, 2016, pp. 187–202.
7. Mercer, C., et al.: A Delamination Mechanism for Thermal Barrier Coatings Subject to Calcium-Magnesium-Alumino-Silicate (CMAS) Infiltration. *Acta Mater.*, vol. 53, 2005, pp. 1029–1039.
8. Kramer, Stephan; Yang, James; and Levi, Carlos G.: Thermochemical Interaction of Thermal Barrier Coatings With Molten CaO-MgO-Al<sub>2</sub>O<sub>3</sub>-SiO<sub>2</sub> (CMAS) Deposits. *J. Am. Ceram. Soc.*, vol. 89, no. 10, 2006, pp. 3167–3175.
9. Grant, Kendra M., et al.: CMAS Degradation of Environmental Barrier Coatings. *Surf. Coat. Technol.*, vol. 202, nos. 4–7, 2007, pp. 653–657.
10. Harder, Bryan J., et al.: Chemical and Mechanical Consequences of Environmental Barrier Coating Exposure to Calcium-Magnesium-Aluminosilicate. *J. Am. Ceram. Soc.*, vol. 94, no. 1, 2011, pp. S178–S185.
11. Levi, Carlos G., et al.: Environmental Degradation of TBCs by Molten Salt. *MRS Bull.*, vol. 37, no. 10, 2012, pp. 932–941.
12. Krause, A.R., et al.: 2ZrO<sub>2</sub>·Y<sub>2</sub>O<sub>3</sub> Thermal Barrier Coatings Resistant to Degradation by Molten CMAS: Part I, Optical Basicity Considerations and Processing. *J. Am. Ceram. Soc.*, vol. 97, no. 12, 2014, pp. 3943–3949.
13. Krause, Amanda R., et al.: 2ZrO<sub>2</sub>·Y<sub>2</sub>O<sub>3</sub> Thermal Barrier Coatings Resistant to Degradation by Molten CMAS: Part II, Interactions With Sand and Fly Ash. *J. Am. Ceram. Soc.*, vol. 97, no. 12, 2014, pp. 3950–3957.
14. Zhu, Dongming; and Miller, Robert A.: Development of Advanced Low Conductivity Thermal Barrier Coatings. *Int. J. Appl. Ceram. Technol.*, vol. 1, no. 1, 2004, pp. 86–94.
15. Zhu, Dongming: NASA's Advanced Environmental Barrier Coatings Development for SiC/SiC Ceramic Matrix Composites: Understanding Calcium Magnesium Alumino-Silicate (CMAS) Degradations and Resistance. GRC-E-DAA-TN15925, 2014.
16. Wiesner, Valerie L.; and Bansal, Narottam P.: Crystallization Kinetics of Calcium-Magnesium Aluminosilicate (CMAS) Glass. *Surf. Coat. Technol.*, vol. 259, part C, 2014, pp. 608–615.
17. Ahlborg, Nadia L.; and Zhu, Dongming: Calcium-Magnesium Aluminosilicate (CMAS) Reactions and Degradation Mechanisms of Advanced Environmental Barrier Coatings. *Surf. Coat. Technol.*, vol. 237, 2013, pp. 79–87.
18. Duffy, J.A.; and Ingram, M.D.: An Interpretation of Glass Chemistry in Terms of Optical Basicity Concept. *J. Non-Cryst. Solids*, vol. 21, no. 3, 1976, pp. 373–410.
19. Duffy, J.A.: Ionic—Covalent Character of Metal and Nonmetal Oxides. *J. Phys. Chem. A*, vol. 110, 2006, pp. 13245–13248.
20. Duffy, J.A.: Optical Basicity Analysis of Glasses Containing Trivalent Scandium, Yttrium, Gallium and Indium. *Phys. Chem. Glasses*, vol. 46, no. 5, 2005, pp. 500–504.

21. Clarke, T.A.; and Rizkalla, E.N.: X-ray Photoelectron Spectroscopy of Some Silicates. *Chem. Phys. Lett.*, vol. 37, no. 3, 1976, pp. 523–526.
22. Duffy, J.A.: Polarisability and Polarising Power of Rare Earth Ions in Glass: An Optical Basicity Assessment. *Phys. Chem. Glasses*, vol. 46, no. 1, 2005, pp. 1–6.
23. Dimitrov, Vesselin; and Sakka, Sumio: Electronic Oxide Polarizability and Optical Basicity of Simple Oxides. *J. Appl. Phys.*, vol. 79, no. 3, 1996, pp. 1736–1740.
24. Costa, Gustavo C.C.; and Jacobson, N.S.: Mass Spectrometric Measurements of the Silica Activity in the  $\text{Yb}_2\text{O}_3\text{-SiO}_2$  System and Implications To Assess the Degradation of Silicate-Based Coatings in Combustion Environments. *J. Eur. Ceram. Soc.*, vol. 35, no. 15, 2015, pp. 4259–4267.
25. Costa, Gustavo C.C.; Xu, Hongwu; and Navrotsky, Alexandra: Thermochemistry of Barium Hollandites. *J. Am. Ceram. Soc.*, vol. 96, no. 5, 2013, pp. 1554–1561.
26. Navrotsky, Alexandra: Energetics of Silicate Melts. *Rev. Miner.*, vol. 32, no. 1, 1995, pp. 121–143.
27. Korytseva, Anastasia; and Navrotsky, Alexandra: High-Temperature Calorimetric Study of Oxide Component Dissolution in a  $\text{CaO-MgO-Al}_2\text{O}_3\text{-SiO}_2$  Slag at 1450 °C. *J. Am. Ceram. Soc.*, vol. 100, no. 3, 2016, pp. 1172–1177.
28. Navrotsky, Alexandra: *Physics and Chemistry of Earth Materials*. Cambridge University Press, Cambridge, UK, 1995.



